Modeling of hybrid graphene/CNT/polymer nanocomposite pressure sensors under bending

Han Du [a], Aaron D. Mazzeo [a], Jerry W. Shan [a], Xiaodong Xia [b], George J. Weng [a, *]
[a] Department of Mechanical and Aerospace Engineering, Rutgers University,
New Brunswick, NJ 08903, USA
[b] School of Civil Engineering, Central South University, Changsha, 410083, PR China

Abstract

The hybrid graphene/carbon nanotube (CNT)/polymer nanocomposite is reported to be an ideal medium that makes up nanofiller-reinforced pressure sensors. In this paper we aim to illustrate the resistance response of such nanocomposite-based piezoresistive sensors under bending. The main idea is that the volume fractions of the two reinforced nano-inclusion phases – graphene and CNTs - change as a result of bending deformation, and this further promotes the overall electrical response of a pressure sensor. To this end, we construct a three-phase composite that simultaneously contains graphene nanoplatelets (GNPs) and CNTs as two inclusion phases and fluorinated elastomer as the matrix. A model of treating a pressure sensor as a thin plate under bending is introduced to analyze its elastic deformation. Then a micromechanics theory for an isotropic composite containing randomly oriented, transversely isotropic ellipsoidal inclusions is adopted to derive the effective elastic moduli for the hybrid composite. The effective-medium approximation (EMA) and resistors in parallel model are subsequently invoked to calculate the overall electrical resistance and to describe how it depends on the applied bending pressure. The calculated resistance reductions are shown to be in close agreement with the experimental data of graphene/CNT/THV sensors under 0 to 1.75 KPa. Several other novel features of the model are also highlighted.

Key words: Nanofiller-reinforced piezoresistive pressure sensor, Graphene/CNT/polymer nanocomposite, Bending deformation, Effective elastic moduli, Electrical conductivity and percolation threshold, Resistors in parallel, Interface effects.

---

*Corresponding author. *E-mail address*: gjweng@soe.rutgers.edu

1 INTRODUCTION

Research on nanofiller-based pressure sensors has been very active in recent years. With the growing demands for healthcare, energy harvest and communications to environment, flexible and wearable pressure sensors are of great demand for various industrial and medical applications. These applications include electronic skin [1-2], touch detection [3], biomedical devices and prostheses [4], human motion monitoring [5] and energy harvesting devices [6]. The working mechanism of pressure sensor can be classified as force-induced capacitive sensing [7], piezoelectric sensing [8], triboelectric sensing [6] and piezoresistive sensing [1,9].

Resistive sensors have great development potential and plenty of promising applications due to easy fabrication, simple structure, and good sensitivity at low pressures (usually less than 5kPa) [10]. There is a strong demand for exploring highly sensitive, self-powered, portable pressure sensors because of the limited working time and environmental pollution. In this case, elastomer-based conductive polymer nanocomposites (CPCs) are popular and commonly used as they possess unique physical properties, high surface area, small dimensions and low cost [11]. Frequently used additives as the conductive phase in CPCs include carbon black (CB), metal nanoparticles, carbon fiber, carbon nanotubes (CNTs) and graphene nanoplatelets. Besides these traditional inclusions, novel microstructures have also been used such as CB-polyurethane (PU) foam [12], graphene-PU foam [13], graphene-polyimides (PIs) foam [14], polypyrrole hydrogel hollow-sphere microstructures [9], hierarchically porous polydimethylsiloxane (PDMS) structures [15], and embossed cellulose-CB paper [16].

Among these nanofiller-based and microstructure-based composite sensors, CNT reinforced nanocomposite sensors are cost-effective and capable of measuring a wide range of pressures. Multi-walled carbon nanotubes (MWCNTs) are available at relatively low cost and they can be bent through large angles and strains without mechanical failure and can resist failure under repeated bending [17]. For applications, Hu et al. [18] developed a multi-scale three-dimensional finite element method (FEM) model to predict the piezoresistivity behavior of CNT/epoxy nanocomposite resistive sensor. Sepúlveda et al. [19]

constructed an experiment where aligned CNTs embedded in a flexible substrate of PDMS, are used to fabricate capacitive sensors for testing blood pressure. It reveals that the bending of sensor caused by variations in outside pressure generates capacitive changes proportional to the pressure change.

Like CNTs, graphene is another alternate low cost and stretchable filler material that has been used to form flexible electronic sensors [5,20]. Graphene shares similar electronic properties as CNTs but is more amenable to patterning and bulk manufacturing through solution-based exfoliation [21]. Yang et al. [22] analyzed graphene/PDMS sensor in sandwiched fabrication by FEM, and found its piezoresistive response decided by the compressibility of the microstructure and contact area. Lou et al. [23] designed and fabricated a highly sensitive piezoresistive pressure sensor by a self-assembled platform that combines a viscoelastic material P(VDF-TrFe) with conductive reduced graphene oxide (rGO). The sensor exhibits low detection limit and working voltage, excellent long-term stability under 100,000 cycles, and rapid response time under low frequency.

Apart from the single-inclusion reinforced nanocomposite sensors, nanocomposite sensors containing multi-inclusion phases have drawn more and more attention. Nowadays graphene/CNT/polymer nanocomposite becomes an ideal functional material to design and fabricate various pressure sensors for purposes of enhancing sensitivity, improving working time and expanding application scope. Hybrid CNT/graphene-based strain sensors were previously reported by Hwang et al. [24], in their experiment the vacuum filtration with dispersion of CNT/graphene is used to form a conductive layer that was subsequently transferred onto a polymethylmethacrylate (PMMA) substrate. The advantages of hybrid CNT/graphene structure are various and significant, for instance, Lee et al. [25] presented strain sensors featuring a piezoresistive composite made from a combination of MWCNTs and GNPs in PDMS to form a screen printable conductive PDMS, and tested zero current resistance and percolation threshold of sensor. Tran et al. [26] constructed quantum resistive pressure sensors consisting of graphene/CNT hybrid architectures, and the sensors are reported to have a more stable piezoresistive behavior with different compression speeds and mechanical histories. A higher range of linear resistive response is also achieved.

The three-phase graphene/CNT/polymer nanocomposite itself exhibits superior properties such as higher electrical conductivity and mechanical flexibility compared to traditional two-phase nanofiller/polymer nanocomposites. The enhancement mechanism from two inclusion phases is more significant and complicated than materials with a single inclusion phase. For example, the influences of adding graphene on CNT/polymer composite are reported by Peng et al. [27], in which they fabricated a cobalt sulfide/reduced graphene-oxide/carbon nanotube (CoS_2/rGO-CNT) nanocomposite. The rGO nanosheets are assembled into a continuous carbon skeleton and entangled into porous CNT networks, yielding a three-dimensional conductive and flexible structural CoS_2/rGO-CNT network. Similarly, the effects of inserting CNTs into graphene/polymer composite can be estimated from Shen et al. [28], where a three-dimensional TiO_2-graphene-CNT nanocomposite is developed. CNTs in this unique hybrid nanostructure not only prevent the restacking and agglomeration of graphene sheets but also provide additional electron-transport paths besides the graphene layers. Both sets of experiment demonstrate that conductive graphene sheets and CNTs and their porous structures are beneficial for electronic and ionic transport, which leads to superior electrical and mechanical properties after the addition of the second inclusion phase.

In the simulation domain, increasing effort has been placed to develop the homogenization scheme to predict the overall behaviors of two-phase inclusion/polymer nanocomposites [29-31]. In addition to the intrinsic properties of nanofillers and polymer matrix, many microstructural features such as filler aspect ratio [29], filler orientation state [30], and filler agglomeration [31], are reported to exert major effects on the overall mechanical and electrical properties, as well as the percolation threshold in electrical conductivity. Although there is substantial amount of research on the properties of two-phase graphene- or CNT-based nanocomposites, there are very few studies that concentrate on the mechanical and electrical properties of three-phase graphene/CNT/polymer nanocomposite. Consideration of such hybrid nanocomposites in pressure sensors remains scarce, if any.

In this article, we will study a piezoresistive sensor based on graphene/CNT/elastomer (fluorinated copolymer) nanocomposite under bending. Our focus is to develop a model for the calculation of effective conductivity and the evaluation of resistance response of the hybrid nanocomposite under an external bending pressure. To this end a bent composite thin plate is first constructed to describe the bending deformation and determine the volume change of the pressure sensor. In this step, the change of Young's modulus of the sensor as a function of bending deformation and applied force will be calculated by invoking the Mori-Tanaka method [32] and Qiu-Weng's theory [33] for an isotropic composite containing transversely isotropic randomly oriented ellipsoidal inclusions. Then the volume fraction changes of graphene and CNT phases during the bending process will be derived. Subsequently, we will call upon the classic Bruggeman's effective-medium approximation (EMA) [34] to evaluate the effective conductivity and, together with the result of effective elastic moduli, to determine the resistance response of the three-phase nanocomposite sensor as a function of the applied bending pressure. At the end, the calculated resistance curves in both graphene/CNT/elastomer-based sensor and CNT/elastomer-based sensor will be compared with experiments.

2 THE THEORY

2.1 Nanofiller reinforced composite bending model

The theory starts with a mechanical bending model of a piezoresistive pressure sensor as shown in Fig. 1. The dark region represents the sensor which is wrapped and embedded by the green substrate, and they are sandwiched between two Au electrodes. The external pressure P is applied perpendicular to the electrodes to make the sensor bend together with the substrate to some extent. To prepare for later comparison with the experimental data of Lee *et al.* [35], the sensor is a three-phase nanocomposite which includes GNPs, CNTs and fluorinated copolymer, tetrafluoroethylene-hexafluoropropylene-vinylidenefluoride (THV). By changing the value of applied pressure and testing the effective resistance of the sensor, the electrical behavior of a pressure sensor under bending can be obtained.

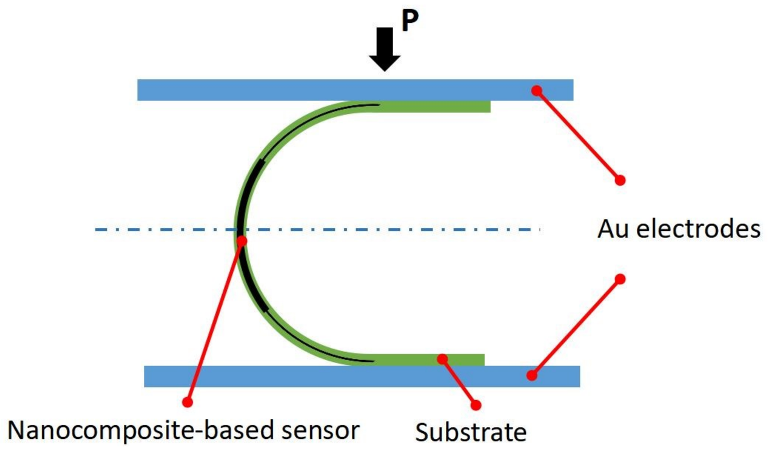

Fig.1. The pressure response measurement of the sensor under bending

To analyze this issue, we treat the sensor as a thin plate with a longitudinal cross section shown in Fig. 2(a). The shadow area is the nanofiller composite and the whole structure is symmetric with respect to the vertical dashed line. The external applied force will cause a resultant normal force N and a resultant moment M that are acting on the cross section of the composite specimen. Similar with the beam bending issue, the top surface is compressed while the bottom one is stretched, so there must be a surface called the neutral surface that does not undergo a change in length. In addition, ρ is the radius of curvature and θ is the angle that spans over the bent composite thin plate. Thus, we have $\rho\theta = L$, where L is the length of the composite sensor. Due to the presence of axial normal force, N, the neutral surface is not located in the symmetric plane as with a pure bending problem.

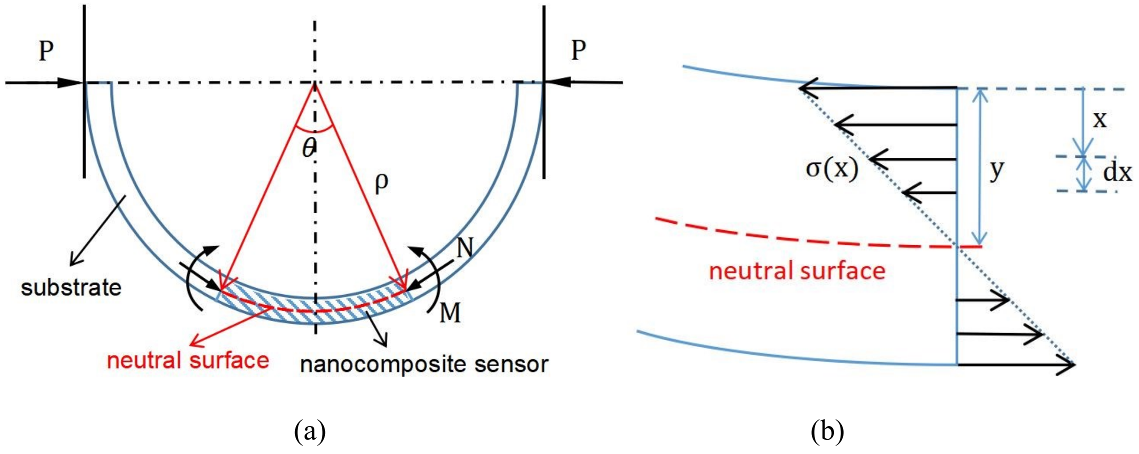

(a) (b)

Fig.2. (a) Longitudinal section of thin plate sensor and (b) cross-sectional internal stress analysis

Then we take the composite cross section to do the stress analysis, as Fig. 2(b) shows. Stress and strain of different horizontal surfaces are functions of x, where x is the vertical distance from these surfaces to the top surface. y is the distance between the neutral surface and the top surface. The stress-strain relationship can be derived from Hooke's law as

$$\sigma(x) = E \cdot \varepsilon(x), \tag{1}$$

where E is Young's modulus of the entire composite under bending. We should notice that, for the composite sensor, its E does not remain constant; it depends on the extent of bending. This is due to the fact that the total volume of composite sensor changes because of bending, and this in turn leads to a change of volume fractions of graphene nanoplatelets and CNTs, which in turn influences the overall elastic moduli of the nanoinclusion/polymer composite. It will be shown at the end of Sect. 2.2.3 that E depends on ρ and y, as $E(\rho, y)$.

Similar to the beam theory, we assume different surfaces have the same curvature, so we have the expression of strains

$$\varepsilon(x) = \frac{[\rho-(y-x)]\theta - \rho\theta}{\rho\theta} = \frac{x-y}{\rho}. \tag{2}$$

Integrating the stress over the cross section with respect to the neutral axis, we can obtain the resultant force and resultant moment by taking tension as positive and compression as negative. On the other hand, from force analysis we can use external pressure and the geometric property of the sector section to express the resultant force and moment. This leads to

$$\int_0^t E(\rho, y)\frac{x-y}{\rho}W dx = -\frac{P}{\cos\frac{\theta}{2}}, \tag{3.1}$$

$$\int_0^t E(\rho, y)\frac{(x-y)^2}{\rho}W dx = P \cdot \rho \cos\frac{\theta}{2}, \tag{3.2}$$

respectively, where W and t are the width and thickness of the composite sensor. Now we have two equations with two unknown variables, ρ (or θ) and y. Their values can be determined explicitly if the size of the nanocomposite-based sensor, (L, W, t), is given and the applied pressure is set. After the value of y is calculated, the position of the neutral surface can be determined. From the definition of neutral surface, the volume always decreases for the part above the neutral surface while volume increases for the part below it. Then according to the assumption, different bent horizontal surfaces have same curvature, and geometric property of the longitudinal section under bending (a sector), we can obtain the volume changes for the parts above and below the neutral surface:

$$\frac{V'_{above}}{V^0_{above}} = \frac{\rho - y/2}{\rho} \tag{4.1}$$

$$\frac{V'_{below}}{V^0_{below}} = \frac{\rho + (t-y)/2}{\rho} \tag{4.2}$$

where V^0_{above}, V^0_{below}, V'_{above} and V'_{below} are volumes of the part above and below neutral surface before and after bending, respectively. Since $0 < y < t$, the first ratio is always less than 1 and the second is larger than 1, which corresponds to neutral surface definition. Furthermore, the ratio of the total composite volume under bending to the initial volume before bending can be obtained as

$$\frac{V'}{V_0} = \frac{\rho - y + t/2}{\rho}, \tag{5}$$

which will be used in the next sections to calculate the updated volume fractions of GNPs and CNTs phases from their initial concentrations under the bending state.

2.2 Homogenization scheme and elastic properties of the graphene/CNT/polymer nanocomposite

Next, we focus on the determination of effective elastic moduli of the nanocomposite itself. It is a three-phase composite containing both graphene nanoplatelets and CNTs simultaneously. This is a novel medium compared to traditional two-phase composites that just have graphene or just have CNTs. In this 3-phase system, and in accordance with the experimental setting of Lee et al. [35] whose data will be compared later, both graphene and CNT fillers are taken to be homogeneously dispersed and randomly oriented inside the THV matrix. A schematic of the three-phase graphene/CNT/THV composite is depicted in Fig. 3.

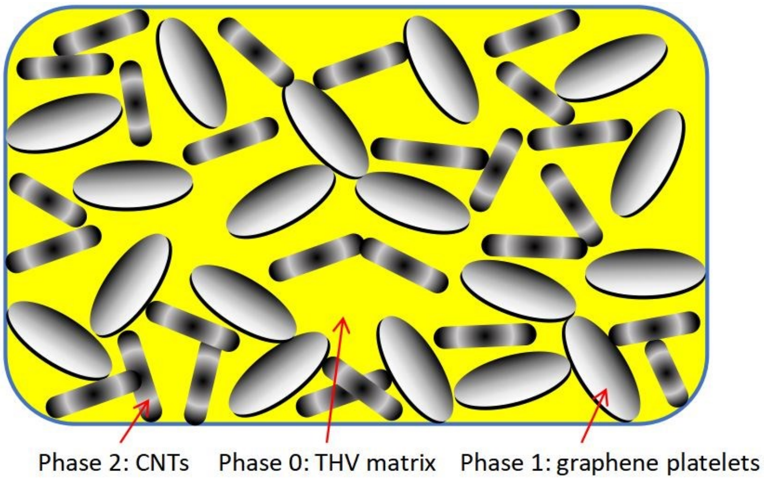

Fig.3. The schematic of the three-phase graphene/CNT/THV composite

2.2.1 Volume fractions of the three constituent phases

In this article, we use phase 0, phase 1 and phase 2 to represent THV matrix phase, graphene nanoplatelets and CNTs respectively. The volume fractions of graphene phase, CNT phase and THV phase are denoted by c_1, c_2 and c_0, in turn. From the previous section we know that pressure-induced bending will cause the volume of the entire composite to change, or more precisely, to decrease. This leads to the changes of volume fractions of each phase inside the composite since we assume the total volume of either graphene fillers or CNTs will not be affected from the bending. Based on this observation, we can establish the expressions of their volume fractions during the bending as

$$c_1 = c_1^{initial} \frac{\rho}{\rho - y + t/2}, \quad \text{for graphene,} \tag{6.1}$$

$$c_2 = c_2^{initial} \frac{\rho}{\rho - y + t/2}, \quad \text{for CNTs,} \tag{6.2}$$

Here $c_1^{initial}$ and $c_2^{initial}$ are the initial volume fractions of graphene and CNTs in the unbent state. The volume fraction of polymer matrix always follows from $c_0 = 1 - c_1 - c_2$.

2.2.2 Elastic stress-strain relations of constituent phases

Graphene nanoplatelets and CNT fillers are both transversely isotropic ellipsoidal inclusions. For graphene, we take the normal-to-plane direction as direction 1 and in-plane isotropic directions as 2 and 3; and for CNT, we take the axial direction as direction 1 and the two transverse directions as 2 and 3. Their transversely stress-strain relations can be succinctly written in Hill's short-hand notations as [36]

$$\boldsymbol{\sigma}^{(1)} = \mathbf{L}_1 \boldsymbol{\varepsilon}^{(1)} \text{ with } \mathbf{L}_1 = (2k_1, l_1, n_1, 2m_1, 2p_1), \tag{7.1}$$

$$\boldsymbol{\sigma}^{(2)} = \mathbf{L}_2 \boldsymbol{\varepsilon}^{(2)} \text{ with } \mathbf{L}_2 = (2k_2, l_2, n_2, 2m_2, 2p_2), \tag{7.2}$$

where $\mathbf{L}_1$ and $\mathbf{L}_2$ are the elastic stiffness tensors of graphene and CNT, the superscript and subscript "1" and "2" represent the graphene and CNT phases. The five constants, k, l, n, m and p are their plane-strain bulk modulus, cross modulus, axial modulus under an axial strain, transverse shear modulus, and axial shear modulus, respectively.

Unlike the graphene or CNTs, the polymer matrix is an isotropic medium. Its isotropic stiffness tensor can be written as $\mathbf{L}_0 = (3\kappa_0, 2\mu_0)$, where subscript "0" represents the polymer phase and κ_0 and μ_0 are its bulk and shear moduli.

2.2.3 The overall effective elastic moduli of the three-phase composite

Even though both graphene and CNTs are transversely isotropic inclusions, they are randomly dispersed inside the composite, which makes the entire composite an isotropic medium. So, the issue can be treated as randomly oriented ellipsoidal inclusions in an isotropic matrix. By means of Mori-Tanaka's method [32], Qiu and Weng [33] developed an orientational scheme to calculate the effective elastic moduli of such composites. The effective moduli tensor of the entire three-phase composite holds the following expression

$$\mathbf{L} = \left(c_0 \mathbf{L}_0 + c_1 \langle \mathbf{L}_1 \mathbf{A}_1 \rangle + c_2 \langle \mathbf{L}_2 \mathbf{A}_2 \rangle \right) \left(c_0 \mathbf{I} + c_1 \langle \mathbf{A}_1 \rangle + c_2 \langle \mathbf{A}_2 \rangle \right)^{-1}, \tag{8}$$

where the curly brackets $\langle \cdot \rangle$ designate the orientational average of the said quantity, and $\mathbf{A}$ is the strain concentration tensor. The orientational average of $\mathbf{A}$ is isotropic, with $\langle \mathbf{A}_i \rangle = \left(3\xi_i^{\mathrm{A}}, 2\eta_i^{\mathrm{A}} \right)$, where $i = 1,2$ for the two inclusion phases. Its hydrostatic and deviatoric components are respectively

$$\xi_i^{\mathrm{A}} = \frac{1}{9l^{(i)}}\left[2d^{(i)} - 2\left(g^{(i)} + h^{(i)}\right) + c^{(i)}\right], \tag{9.1}$$

$$\eta_i^{\mathrm{A}} = \frac{1}{30l^{(i)}}\left[d^{(i)} + 2\left(g^{(i)} + h^{(i)}\right) + 2c^{(i)}\right] + \frac{1}{5}\left(\frac{1}{e^{(i)}} + \frac{1}{f^{(i)}}\right). \tag{9.2}$$

Similarly, we write $\langle \mathbf{L}_i \mathbf{A}_i \rangle = \left(3\xi_i^{\mathrm{LA}}, 2\eta_i^{\mathrm{LA}}\right)$, and its components are

$$\xi_i^{\mathrm{LA}} = \frac{1}{9l^{(i)}}\left[4\left(k_i d^{(i)} - l_i g^{(i)}\right) + 2\left(l_i d^{(i)} - n_i g^{(i)} + l_i c^{(i)} - 2k_i h^{(i)}\right) + \left(n_i c^{(i)} - 2l_i h^{(i)}\right)\right] \tag{10.1}$$

$$\eta_i^{\mathrm{LA}} = \frac{1}{15l^{(i)}}\left[\left(k_i d^{(i)} - l_i g^{(i)}\right) - \left(l_i d^{(i)} - n_i g^{(i)} + l_i c^{(i)} - 2k_i h^{(i)}\right) + \left(n_i c^{(i)} - 2l_i h^{(i)}\right)\right] + \frac{2}{5}\left(\frac{m_i}{e^{(i)}} + \frac{p_i}{f^{(i)}}\right) \tag{10.2}$$

In above equations, $i = 1, 2$ represent the graphene phase and CNT phase respectively. The parameters for circular thin disc-like graphene are given as $c^{(1)} = 1$, $d^{(1)} = n_1 / n_0$, $e^{(1)} = 1$, $f^{(1)} = p_1 / p_0$, $g^{(1)} = (l_1 - l_0)/n_0$, $h^{(1)} = 0$ and $l^{(1)} = n_1 / n_0$; for a long circular cylinder-like CNT they are given as $c^{(2)} = 1 + (k_2 - k_0)/n_0$, $d^{(2)} = 1$, $e^{(2)} = 1 + (m_0 + n_0)(m_2 - m_0)/(2m_0 n_0)$, $f^{(2)} = (p_2 + p_0)/(2p_0)$, $g^{(2)} = 0$, $h^{(2)} = (l_2 - l_0)/(2n_0)$ and $l^{(2)} = 1 + (k_2 - k_0)/n_0$.

The effective stiffness tensor of entire composite follows Eq. (8), $\mathbf{L} = (3\kappa, 2\mu)$, with

$$\kappa = \frac{c_0\kappa_0 + c_1\xi_1^{\mathrm{LA}} + c_2\xi_2^{\mathrm{LA}}}{c_0 + 3c_1\xi_1^{\mathrm{A}} + 3c_2\xi_2^{\mathrm{A}}}, \quad \mu = \frac{c_0\mu_0 + c_1\eta_1^{\mathrm{LA}} + c_2\eta_2^{\mathrm{LA}}}{c_0 + 2c_1\eta_1^{\mathrm{A}} + 2c_2\eta_2^{\mathrm{A}}}. \tag{11}$$

Eq. (11) renders the end results of the effective bulk and shear moduli of the 3-phase graphene/CNT/polymer composite at given filler concentrations, c_1 and c_2. These filler concentrations are evaluated at the bent state of the pressure sensor, which are related to the initial concentrations in the unbent state from Eqs. (6.1) and (6.2). The corresponding Young's modulus can be written in terms of the bulk and shear moduli, leading to

$$E = \frac{9\kappa\mu}{3\kappa + \mu} = E(c_1, c_2), \quad \text{or} \quad E = E(c_1^{initial}, c_2^{initial}, \rho, y), \quad \text{from Eqs. (6.1) and (6.2).} \tag{12}$$

This Young's modulus is exactly what we need in Eq. (1). It is evident now that the Young's modulus of the sensor is not a constant; it is a function of ρ and y as we pointed out in Sect. 2.1.

2.2.4 The imperfect mechanical bonding between phases

The preceding results have been obtained with a perfect interface condition. However, the true nanofiller-polymer interface is usually not perfect, which tends to lower the overall elastic stiffness. A "coated filler" is introduced here with a thin interphase to treat the weakening effect of an imperfect interface, as Fig. 4 shows. The Mori-Tanaka model is adopted to obtain the effective elastic stiffness tensor of one coated filler, $\mathbf{L}_c$. By assuming the properties of the interface to be isotropic, the elastic stiffness tensors of a coated graphene nanoplatelet and CNT can be evaluated as [37]

$$\mathbf{L}_c^{GNP} = \mathbf{L}_{\text{int}}^{GNP} \left\{ \left(1 - c_{\text{int}}^{GNP}\right) \left[c_{\text{int}}^{GNP} \mathbf{S}_{\text{int}}^{GNP} + \left(\mathbf{L}_1 - \mathbf{L}_{\text{int}}^{GNP}\right)^{-1} \mathbf{L}_{\text{int}}^{GNP} \right] + \mathbf{I} \right\}, \tag{13.1}$$

$$\mathbf{L}_c^{CNT} = \mathbf{L}_{\text{int}}^{CNT} \left\{ \left(1 - c_{\text{int}}^{CNT}\right) \left[c_{\text{int}}^{CNT} \mathbf{S}_{\text{int}}^{CNT} + \left(\mathbf{L}_2 - \mathbf{L}_{\text{int}}^{CNT}\right)^{-1} \mathbf{L}_{\text{int}}^{CNT} \right] + \mathbf{I} \right\}, \tag{13.2}$$

where $\mathbf{L}_c = (2k_c, l_c, n_c, 2m_c, 2p_c)$, with the subscript "c" representing the "coated" inclusion. In addition, c_{int} is the volume fraction of the interphase in one coated graphene platelet or one coated CNT. With graphene platelet,

$$c_{\text{int}}^{GNP} = 1 - \frac{\lambda}{2}\left(\frac{\lambda}{2\alpha_1}\right)^2 \Bigg/ \left[\left(\frac{\lambda}{2} + h^{GNP}\right)\left(\frac{\lambda}{2\alpha_1} + h^{GNP}\right)^2 \right], \tag{14.1}$$

and with CNT,

$$c_{\text{int}}^{CNT} = 1 - \left(\alpha_2 R^3\right) \Big/ \left[\left(R + h^{CNT}\right)^2 \left(\alpha_2 R + h^{CNT}\right) \right], \tag{14.2}$$

where h^{GNP} and h^{CNT} are graphene-matrix interlayer thickness and CNT-matrix interlayer thickness, respectively. λ is the thickness of the graphene platelets, and R is the radius of the CNTs. α_1 and α_2 are aspect ratios of graphene and CNT, with $\alpha_1 << 1$, and $\alpha_2 >> 1$. For simplicity we take $c_{\text{int}}^{GNP} = c_{\text{int}}^{CNT} = 0.1$ in the calculations.

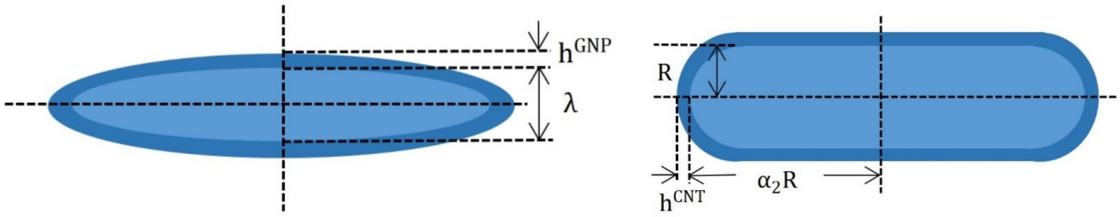

(a) (b)

Fig.4. (a) A coated graphene platelet and (b) a coated CNT filler

In addition, tensor $\mathbf{S}_{\text{int}} = (S_{2222}^{(\text{int})} + S_{2233}^{(\text{int})}, S_{1122}^{(\text{int})}, S_{2211}^{(\text{int})}, S_{1111}^{(\text{int})}, 2S_{2323}^{(\text{int})}, 2S_{1212}^{(\text{int})})$ is the Eshelby S-tensor of coated filler, and $\mathbf{I} = (1,0,0,1,1,1)$ is the unit tensor written in the transversely isotropic form. The elements of $\mathbf{S}_{\text{int}}^{GNP}$ and $\mathbf{S}_{\text{int}}^{CNT}$ can be obtained from Eqs. (A.1) to (A.7) by replacing ν_0 by ν_{int}^{GNP} and ν_{int}^{CNT}. Furthermore, $\mathbf{L}_{\text{int}}^{GNP}$ and $\mathbf{L}_{\text{int}}^{CNT}$ are elastic moduli tensors of isotropic graphene-THV interfaces and CNT-THV interfaces; their elements can be derived from Appendix Eqs. (A.8) to (A.11).

After considering the influence of imperfect interlayers, the stiffness tensors of graphene and CNT, $\mathbf{L}_1$ and $\mathbf{L}_2$ in Eq. (8) should be replaced by $\mathbf{L}_c^{GNP}$ and $\mathbf{L}_c^{CNT}$ respectively to calculate the overall elastic moduli of the three-phase composite with imperfect interfaces.

2.3 Electrical properties of the graphene/CNT/polymer nanocomposite

From the derived elastic properties of the three-phase composite and the relationship between bending deformation and elastic moduli, we can find out how graphene and CNT volume fractions change under bending. In this section, we discuss the characteristics of the overall electrical properties - especially the conductivity and percolation threshold – of the three-phase composite during the bending process.

2.3.1 Effective-medium approximation (EMA) method

The electrical properties of the three-phase composite in which both graphene and CNT fillers are randomly oriented simultaneously can be analyzed by the effective-medium approximation (EMA). To pave the way for the calculation, we first recall its basic framework under the perfect interface condition. The original effective-medium approximation was developed by Bruggeman [34] and first applied by Landauer [38] to calculate the electrical conductivity of isotropic composites containing perfectly bonded spherical particles. To apply it to either graphene or CNT fillers, or the combination of the two, it is essential to extend it to configurations of ellipsoidal inclusions. There are several ways to extend the original EMA to composites containing aligned or randomly oriented ellipsoidal inclusions with a perfect interface. One of the most convenient ways is to adopt Maxwell's approach of far-field matching as put forward in Weng [39]. This approach requires that the sum of the scattered fields by all constituent phases at far distance be equal to the scattering field of the effective medium itself. If we take the moduli tensor as the conductivity tensor $\boldsymbol{\chi}$, this would lead to the overall effective conductivity $\boldsymbol{\chi}_e$ of the three-phase medium as

$$c_0\left[(\boldsymbol{\chi}_0-\boldsymbol{\chi}_e)^{-1}+\mathbf{S}_0\boldsymbol{\chi}_e^{-1}\right]^{-1}+c_1\left\langle\left[(\boldsymbol{\chi}_1-\boldsymbol{\chi}_e)^{-1}+\mathbf{S}_1\boldsymbol{\chi}_e^{-1}\right]^{-1}\right\rangle+c_2\left\langle\left[(\boldsymbol{\chi}_2-\boldsymbol{\chi}_e)^{-1}+\mathbf{S}_2\boldsymbol{\chi}_e^{-1}\right]^{-1}\right\rangle=\mathbf{0} \qquad (15)$$

where $\langle\cdot\rangle$ stands for the orientational average of the inside quantity as in the previous mechanical section. The quantities $\boldsymbol{\chi}_0$, $\boldsymbol{\chi}_1$ and $\boldsymbol{\chi}_2$ are conductivity tensors of polymer matrix, graphene filler and CNT filler respectively, and $\mathbf{S}_i$ is the depolarization tensor in electrostatics [40] (akin to Eshelby S-tensor in elasticity) for phase *i*. After carrying out the orientational averages for all graphene and CNT fillers, the above equation can be written in a scalar form for the effective conductivity, χ_e, of the three-phase composite

$$\begin{aligned}&c_0\frac{\chi_0-\chi_e}{\chi_e+(1/3)(\chi_0-\chi_e)}+c_1\frac{1}{3}\left[\frac{\chi_1^{GNP}-\chi_e}{\chi_e+S_{11}^{GNP}\left(\chi_1^{GNP}-\chi_e\right)}+\frac{2\left(\chi_3^{GNP}-\chi_e\right)}{\chi_e+S_{33}^{GNP}\left(\chi_3^{GNP}-\chi_e\right)}\right]\\&+c_2\frac{1}{3}\left[\frac{\chi_1^{CNT}-\chi_e}{\chi_e+S_{11}^{CNT}\left(\chi_1^{CNT}-\chi_e\right)}+\frac{2\left(\chi_3^{CNT}-\chi_e\right)}{\chi_e+S_{33}^{CNT}\left(\chi_3^{CNT}-\chi_e\right)}\right]=0.\end{aligned} \qquad (16)$$

In this expression, it is to be recalled that, for graphene platelet, the normal-to-plane direction is 1 and the two in-plane directions are 2 and 3, and that, for CNTs, the axial direction is 1 and the two transverse directions are 2 and 3. Here χ_1^{GNP}, χ_1^{CNT}, χ_3^{GNP} and χ_3^{CNT} are graphene and CNT conductivities along 1 and 3 directions, respectively.

For oblate inclusions such as graphene, the S-tensor has the following components

$$S_{22}^{GNP} = S_{33}^{GNP} = \frac{\alpha_1}{2(1-\alpha_1{}^2)^{3/2}}\left[\arccos\alpha_1 - \alpha_1(1-\alpha_1{}^2)^{1/2}\right], \quad S_{11}^{GNP} = 1 - 2S_{33}^{GNP}, \tag{17}$$

and for prolate inclusions such as CNTs, the components are given by

$$S_{22}^{CNT} = S_{33}^{CNT} = \frac{\alpha_2}{2(\alpha_2{}^2-1)^{3/2}}\left[\alpha_2(\alpha_2{}^2-1)^{1/2} - \operatorname{arc\,cosh}\alpha_2\right], \quad S_{11}^{CNT} = 1 - 2S_{33}^{CNT}, \tag{18}$$

in which α_1 stands for the aspect ratio of phase 1 (graphene platelet) and α_2 is the aspect ratio of phase 2 (CNTs).

2.3.2 Interface effects

As in elastic deformation, the interface effects are important in electrical conduction. For the effective conductivity, there are two principal interface effects. The first one is the imperfect mechanical bonding and the second one is electron tunneling. The first one tends to reduce the overall conductivity while the second one can enhance it.

(i) Imperfect mechanical bonding

As with the study of effective stiffness in the previous section, a thin interphase layer with weak conductivity is introduced here to surround the nanofiller to form a “coated” inclusion. The effective conductivity of the “coated” graphene nanoplatelet and “coated” CNT filler can be derived by the Mori-Tanaka method [32, 37], as

$$\left(\chi_i^{(c)}\right)_{GNP} = \chi_{\text{int}}^{GNP}\left[1 + \frac{(1-c_{\text{int}}^{GNP})\left(\chi_i^{GNP} - \chi_{\text{int}}^{GNP}\right)}{c_{\text{int}}^{GNP}S_{ii}^{GNP}\left(\chi_i^{GNP} - \chi_{\text{int}}^{GNP}\right) + \chi_{\text{int}}^{GNP}}\right], \quad (i = 1,3) \tag{19.1}$$

$$\left(\chi_i^{(c)}\right)_{CNT} = \chi_{\text{int}}^{CNT}\left[1 + \frac{(1-c_{\text{int}}^{CNT})\left(\chi_i^{CNT} - \chi_{\text{int}}^{CNT}\right)}{c_{\text{int}}^{CNT}S_{ii}^{CNT}\left(\chi_i^{CNT} - \chi_{\text{int}}^{CNT}\right) + \chi_{\text{int}}^{CNT}}\right], \quad (i = 1,3) \tag{19.2}$$

where the subscript “*i*” signifies the *i*-th component of the designated quantity, and “int” refers to the thin interphase layer. The quantities, χ_{int}^{GNP} and χ_{int}^{CNT}, are the interphase conductivities between graphene-polymer interphase and between CNT-polymer interphase, that depend on the tunneling-assisted interfacial conductivity.

(ii) Electron tunneling at the interface

To model the tunneling-assisted interfacial conductivity, it was observed that this mechanism leads to a sharp increase in electrical conductivity at the percolation threshold. Near the percolation threshold, the distance between nanofillers markedly decreases, and this increases the probability of electron tunneling. Considering electron hopping as a continuum statistical process, Cauchy's cumulative probability function and its associated resistance-like function have been introduced [29]. In terms of graphene and CNT volume fractions, c_1 and c_2, and their corresponding percolation thresholds, c_1^* and c_2^*, Cauchy's cumulative functions for graphene and CNT nanocomposites are respectively given by

$$F_1\left(c_1,c_1^*,\gamma\right)=\frac{1}{\pi}\arctan\left(\frac{c_1-c_1^*}{\gamma_1}\right)+\frac{1}{2}, \tag{20.1}$$

$$F_2\left(c_2,c_2^*,\gamma\right)=\frac{1}{\pi}\arctan\left(\frac{c_2-c_2^*}{\gamma_2}\right)+\frac{1}{2}, \tag{20.2}$$

where γ_1 and γ_2 are the scale parameters of the electronic tunneling at graphene-matrix interface and CNT-matrix interface, respectively. The resistance-like functions for graphene and CNT are given by

$$\tau_1\left(c_1,c_1^*,\gamma_1\right)=\frac{F_1\left(1,c_1^*,\gamma_1\right)-F_1\left(c_1,c_1^*,\gamma_1\right)}{F_1\left(1,c_1^*,\gamma_1\right)-F_1\left(0,c_1^*,\gamma_1\right)}, \tag{21.1}$$

$$\tau_2\left(c_2,c_2^*,\gamma_2\right)=\frac{F_2\left(1,c_2^*,\gamma_2\right)-F_2\left(c_2,c_2^*,\gamma_2\right)}{F_2\left(1,c_2^*,\gamma_2\right)-F_2\left(0,c_2^*,\gamma_2\right)}. \tag{21.2}$$

With the aid of these two functions, it has been demonstrated that the tunneling-assisted interfacial conductivities can be represented by [29, 30]

$$\chi_{\text{int}}^{GNP}=\chi_0^{(\text{int})GNP}/\tau_1\left(c_1,c_1^*,\gamma_1\right), \tag{22.1}$$

$$\chi_{\text{int}}^{CNT}=\chi_0^{(\text{int})CNT}/\tau_2\left(c_2,c_2^*,\gamma_2\right), \tag{22.2}$$

where $\chi_0^{(\text{int})GNP}$ and $\chi_0^{(\text{int})CNT}$ represent the intrinsic graphene-THV and CNT-THV interfacial conductivities solely due to the imperfect mechanical bonding. This set of interphase conductivities, χ_{int}^{GNP} and χ_{int}^{CNT}, should be used in Eqs. (19.1) and (19.2), to calculate the effective conductivities of the coated graphene and CNT, which in turn are to replace their original conductivities in Eq. (16) of EMA.

2.3.3 Percolation thresholds for the two inclusion phases

Percolation phenomenon occurs in electrical conductivity of nanofiller-reinforced composites. It describes a dramatic increase (usually several orders of magnitude) in conductivity with only a slight increase in the amount of nanofillers. For a traditional two-phase nanocomposite, such as graphene/polymer composite or CNT/polymer composite, the filler aspect ratio, orientation, and dispersion state are reported to be the most important factors affecting the value of percolation threshold.

For our graphene/CNT/polymer three-phase composite, percolation can occur in a graphene/polymer inclusion first, or in a CNT/polymer inclusion first, depending on the aspect ratio of graphene and CNT. So, there are dual percolation phenomena for the three-phase composite. As pointed out in [29], the percolation threshold for each inclusion phase can be determined by setting the matrix phase to be an ideal insulator, $\chi_0 = 0$. Under this condition the governing equation in the EMA, Eq. (16), will turn into a quadratic equation about effective conductivity χ_e. As the graphene volume fraction increases from zero to a critical value c_1^* and CNT volume fraction increases from zero to a critical value c_2^*, this quadratic equation changes from having no solution to giving rise to a non-zero solution. These critical values c_1^* and c_2^* are the percolation thresholds respectively for graphene nanoplatelets and CNTs; they can be determined by setting 0th term of χ_e to zero. Then we can have a linear equation about c_1 and c_2, which means the percolation threshold for one inclusion phase will be influenced by the presence of the other inclusion phase in our three-phase nanocomposite. Only if the volume fraction of one inclusion phase is specified, the percolation threshold for the other one can be derived. The outcomes of the two percolation thresholds are:

$$c_1^* = \frac{9\left[S_{11}^{GNP}-(S_{11}^{GNP})^2\right]\left[S_{11}^{CNT}-(S_{11}^{CNT})^2\right]-c_2\left[S_{11}^{GNP}-(S_{11}^{GNP})^2\right]\left[-9(S_{11}^{CNT})^2+15S_{11}^{CNT}+2\right]}{\left[S_{11}^{CNT}-(S_{11}^{CNT})^2\right]\left[-9(S_{11}^{GNP})^2+15S_{11}^{GNP}+2\right]} \quad (23)$$

$$c_2^* = \frac{9\left[S_{11}^{GNP}-(S_{11}^{GNP})^2\right]\left[S_{11}^{CNT}-(S_{11}^{CNT})^2\right]-c_1\left[S_{11}^{CNT}-(S_{11}^{CNT})^2\right]\left[-9(S_{11}^{GNP})^2+15S_{11}^{GNP}+2\right]}{\left[S_{11}^{GNP}-(S_{11}^{GNP})^2\right]\left[-9(S_{11}^{CNT})^2+15S_{11}^{CNT}+2\right]} \quad (24)$$

We can see unlike the percolation threshold in a two-phase composite that just depends on inclusion aspect ratio, $c_1^* = c_1^*(\alpha)$, percolation threshold for two inclusion phases in three-phase composite is a function as $c_1^* = c_1^*(\alpha_1, \alpha_2, c_2)$ and $c_2^* = c_2^*(\alpha_1, \alpha_2, c_1)$. Moreover, if we take graphene percolation threshold c_1^* for example to consider, CNT volume fraction will make it decrease linearly. This is because after the addition of CNTs in the composite, the space for graphene fillers to form continuous conductive paths are constrained and reduced, besides this, CNTs themselves can connect graphene fillers to construct new graphene-CNT conductive paths. This leads to a lesser amount of graphene required to form the conductive pathway, and thus a lower percolation threshold. The same mechanism also applies to the CNT percolation threshold c_2^*.

2.3.4 Resistors in parallel model for the effective resistance of a pressure sensor

The effective conductivity of three-phase composite χ_e can be determined from EMA and interface effects. For the calculation of overall effective resistance, this bent pressure sensor is treated as numerous differential resistors in parallel as Fig. 5 shows. We divide the sensor plate into n equal small resistors, each resistor holding the length $len_i = L(\rho - y + t \cdot i / n) / \rho$ and cross-sectional area $A = Wt/n$. Here the resistor number i is counted from the top to the bottom so that, $i = 0$ and $i = n$, respectively stand for the top and the bottom layers of the resistors. The resistance of each small resistor is $R_i = len_i / (\chi_e A)$. Finally, the total resistance of the bent pressure sensor can be obtained from the effective resistance of the parallel resistors: $R=\left(\sum_{i=1}^{n}\frac{1}{R_i}\right)^{-1}$. Here we take $n=100$ for calculations in this article.

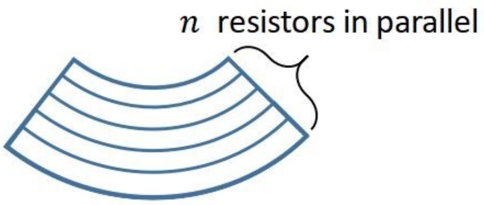

Fig.5. Resistors in parallel model

2.3.5 Computational procedure

By now the theory is completely developed. The following schematic shows the computational procedure for the calculation of final resistance response of the nanocomposite-based piezoresistive sensor, which corresponds to Sect. 2.1 to Sect. 2.3.4.

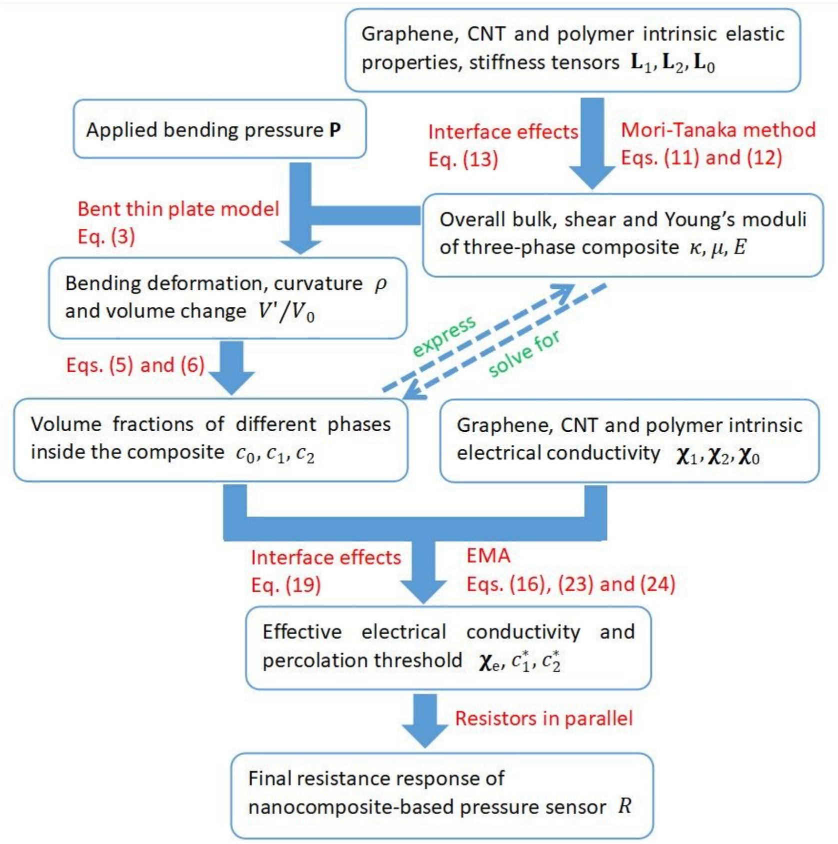

Fig.6. The computational procedure of resistance calculation

3 RESULTS AND DISCUSSION

In order to make direct comparison with the experimental results of Lee et al. [35], the data of the size of pressure sensor were taken directly from that paper, that is, the length $L=9cm$, width $W=9cm$ and thickness $t=20\mu m$. Also, in accordance with the experimental conditions, the aspect ratios of graphene nanoplatelets and CNTs are respectively given as $\alpha_1=0.087$ and $\alpha_2=30.2$. The initial volume fractions of graphene and CNTs before bending are 1.47vol% and 0.026vol%, which were translated from the experiment weight fractions 1.7wt% and 0.017wt%. As for the THV matrix phase, its Young's modulus and Poisson's ratio are $E_0=2\text{GPa}$ and $\nu_0=0.35$. The electrical conductivity of pure THV is taken as $\chi_0=4\times10^{-8}$ S/m. All other mechanical and electrical constants for the calculations of graphene/CNT/THV composite are listed in Tables 1 and 2, respectively.

3.1 Elastic behavior and Young's modulus of graphene/CNT/THV nanocomposite

We first discuss the elastic moduli, especially Young's modulus of the three-phase graphene/CNT/polymer composite, since in bending deformation Young's modulus is an important quantity that correlates stress and strain. From Sect. 2.2.3 we know the overall Young's modulus is a function of volume fractions of two inclusion phases. But we can start with finding how it is solely related to c_1 (or c_2) by specifying different values of c_2 (or c_1). For example, as in original composite before bending, the CNT volume fraction is 0.026%, by setting $c_2=0.026\%$ we draw a curve of $E=E(c_1)$, as Fig. 7(a) shows. The blue solid line is obtained by considering the imperfect interface effect while the red dashed line is the perfect interface result. There is another green dashed line for comparison which represents a condition with no CNT inclusions. We can see that the imperfect mechanical bonding between inclusions and polymer weakens the overall Young's modulus, corresponding to what we discussed in previous theoretical parts. As the amount of CNT inclusions in our three-phase composite is very small, it leads to a small difference with and without CNTs. Similarly, we can get the curve of $E = E(c_2)$ by setting $c_1 = 1.47\%$ before bending, as Fig. 7(b) shows. There is an obvious increase of Young's modulus in the three-phase composite compared to the two-phase one without any graphene because the amount of graphene fillers is much larger than CNTs and graphene plays a dominant role in determining the overall stiffness.

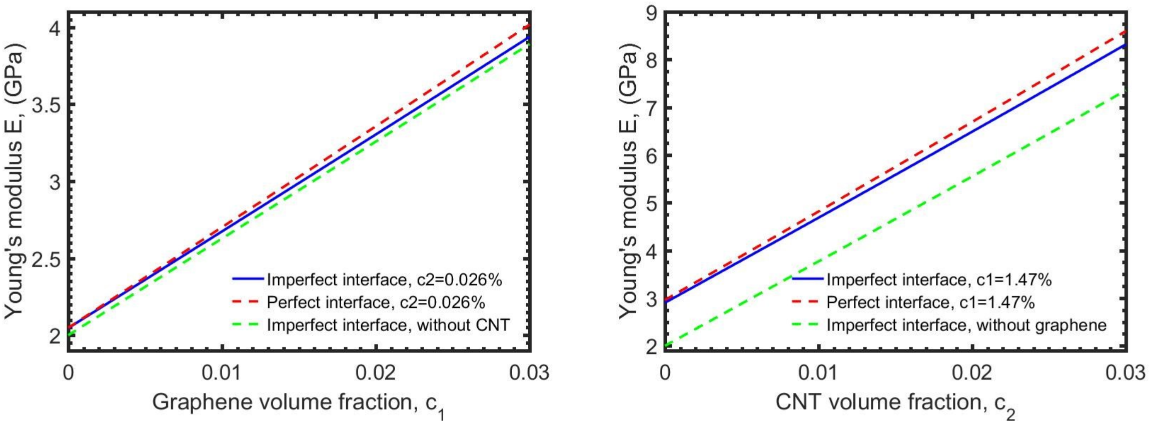

(a) (b)

Fig.7. Overall Young's modulus versus (a) graphene volume fraction and (b) CNT volume fraction

Then we can combine these two to draw a 3D mesh diagram of overall Young's modulus as a function of graphene volume fraction and CNT volume fraction, $E = E(c_1, c_2)$, as Fig. 8 shows. Where the starting point of the surface is 2GPa, corresponds to the Young's modulus of pure polymer. With the increase of either graphene volume fraction or CNT volume fraction, the overall Young's modulus increases smoothly. Besides, we can compare the reinforcements in three-phase nanocomposite from graphene fillers and CNTs, the latter has a more significant enhancement. But this is not a general situation, the reinforcements from different nanofiller inclusions depend on elastic stiffness tensors and aspect ratios of inclusions. With the values we set as in Table 1, under this circumstance we can say CNTs increase the overall elastic moduli to a greater extent than graphene with the same volume fractions.

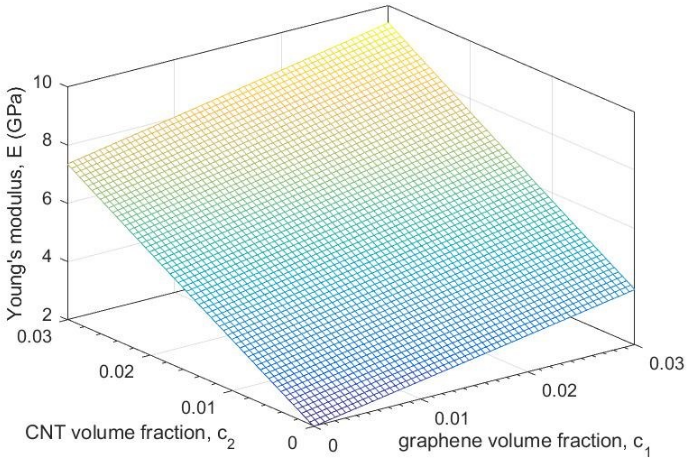

Fig.8. The 3D mesh diagram of Young's modulus versus two inclusion phase volume fractions

3.2 Bending deformation of graphene/CNT/THV nanocomposite

Now we want to find out how the nanofiller pressure sensor deforms under bending. We will give the results by the curvature of bent composite plate and the changes of volume fractions of different phases during the bending process. Since we treat the nanofiller composite as a thin plate and bent composite longitudinal section as a thin-sector, the curvature is a key factor to describe the bending deformation. Combining Young's modulus that we just discussed and bending governing equations in Sect. 2.1, we can solve for the value of radius of curvature ρ explicitly with a given external pressure. Then taking its reciprocal we can get the bending curvature as Fig. 9 shows. There are two conditions that should be taken into account: a variable Young's modulus that is related to pressure $E(P)$ and the imperfect interface. With these two factors, the calculation leads to our solid blue curve. If we treat Young's modulus as a constant value, say the Young's modulus of composite before bending, E_{before}, we will get a curvature that is a little bigger than the true one as the green dashed curve shows. This is because during the bending, the increase of inclusions volume fractions leads to the increase of the effective Young's modulus, making the bent composite stiffer and finally having a little smaller curvature compared to the condition with a constant Young's modulus. As for the interface effect, a perfect interface will lead to a higher Young's modulus, making the curvature smaller than the actual value, as the red dashed curve shows.

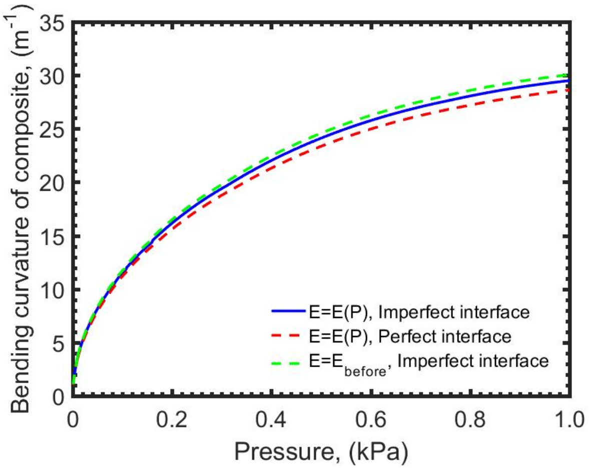

Fig.9. The change in curvature of composite plate under bending

Next, we consider the changes of volume fractions of two inclusion phases, graphene and CNT, during the bending, as Fig. 10 shows. The starting points are respectively the initial graphene volume fraction and CNT volume fraction. With the increase of the applied pressure, the composite becomes more bent, leading to the decrease of the overall volume and increases of graphene or CNT volume fractions. When the applied bending pressure is up to 1kPa, c_1 reaches approximately to 1.487% while c_2 is around 0.0263%. As with the curvature discussion, there are two comparison curves for just considering the imperfect interface or just considering variable Young's modulus.

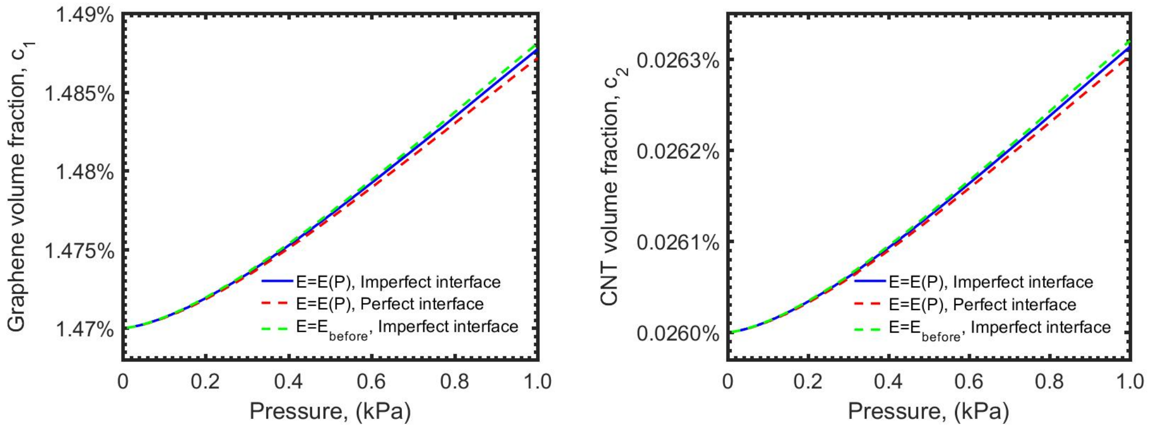

(a) (b)

Fig.10. The change in (a) graphene volume fraction and (b) CNT volume fraction under bending

3.3 Electrical behavior of graphene/CNT/THV nanocomposite

3.3.1 Conductivity and percolation threshold

From EMA, the effective electrical conductivity can be written as a function of inclusions volume fractions, $\chi_e = \chi_e(c_1, c_2)$. The electrical behaviors are more complicated than mechanical ones since the percolation threshold should be considered here, which depends on the two inclusion phases in a three-phase composite. To analyze how graphene phase and CNT phase influence the total effective conductivity, we start by specifying the volume fraction of one phase to find the relation between conductivity and the volume fraction of the other phase.

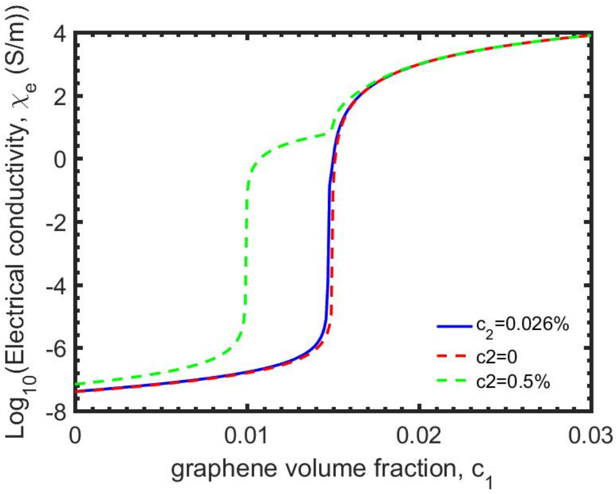

Fig.11. Effective electrical conductivity versus graphene volume fraction at different CNT fractions.

For example, by taking CNT volume fraction at its initial value 0.026%, we can draw a curve of conductivity χ_e versus graphene volume fraction c_1 as in Fig. 11. The blue curve takes both imperfect mechanical bonding interface effect and tunneling assisted interfacial conductivity into account. In the same figure the other two dashed curves that represent $c_2 = 0$ and $c_2 = 0.5\%$ are also provided for us to see how the amount of CNTs affects the percolation threshold of graphene (i.e., the volume fraction of graphene at vertical line). With the increase of CNTs, percolation threshold of graphene will decrease. It corresponds with our Eqs. (23) and (24) where we wrote the percolation threshold of one inclusion phase as a function of volume fraction of the other inclusion phase, $c_1^*(c_2)$. The same rule also applies to the percolation threshold of CNTs with the change of amount of graphene fillers, $c_2^*(c_1)$.

Extending this to the general two-phase-dependent case, the overall conductivity versus volume fractions of the two inclusion phases is described as a 3D mesh diagram in Fig. 12. We can clearly see how exactly percolation occurs inside the graphene/CNT/polymer composite owing to the increase of graphene fillers and CNTs. As for the small jumps of conductivity after percolation, it is attributed to the difference of graphene and CNT intrinsic conductivities, leading to different effective conductivities after percolation in the composite.

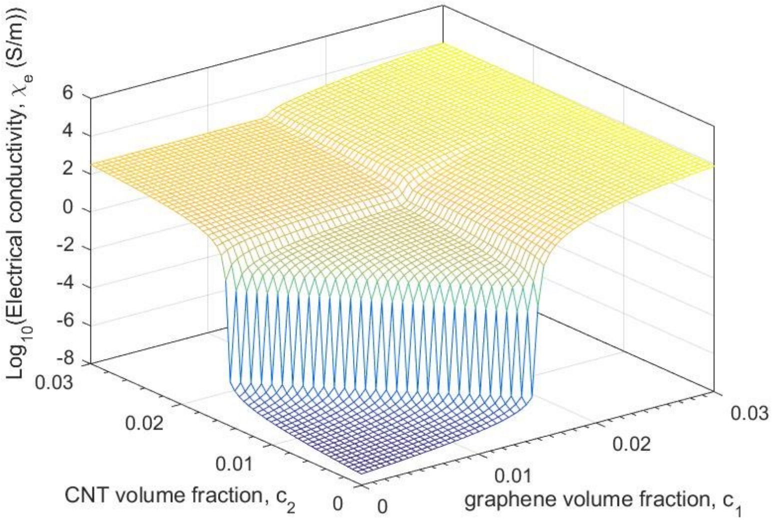

Fig.12. The 3D mesh diagram of electrical conductivity versus two inclusion phase volume fractions

3.3.2 Overall effective resistance

Combining all the above, we finally obtain the relationship between the overall resistance of the three-phase nanocomposite sensor and applied bending pressure. The curves are shown in Fig. 13. The blue points are the experiment data of Lee et al. [35], and the blue solid curve is our analytical result considering imperfect interface and tunneling-assistant interfacial conductivity. From the results we can see that our simulation is in close agreement with the experiment data even though there exist small deviations when the resistance has a sharp decrease. This sharp decrease region is exactly the percolation threshold, which represents that, just after the addition of applied pressure, percolation occurs in graphene/CNT/polymer. Since the amount of CNTs inside the composite is much smaller than graphene, it is graphene that dominants the overall percolation threshold. So, we can conclude that the percolation threshold for graphene, c_1^*, is just slightly larger than the initial graphene volume fraction 1.47%, which corresponds to the applied pressure of 0.1 kPa from our calculations. This value of pressure is close to what can see from the experiment data in [35], which is around 0.1-0.2 kPa.

The green dashed curve and red dashed curve are also provided as two comparison conditions. The first one was obtained by just considering imperfect interface but not the tunneling-assisted conductivity, and the second one is for the perfect interface condition. From the figure we can see that imperfect interface with constant interfacial conductivity will give a little higher resistance, while not considering the imperfect interface will reach a much lower resistance. This is consistent with our results in Sect. 2.3.2.

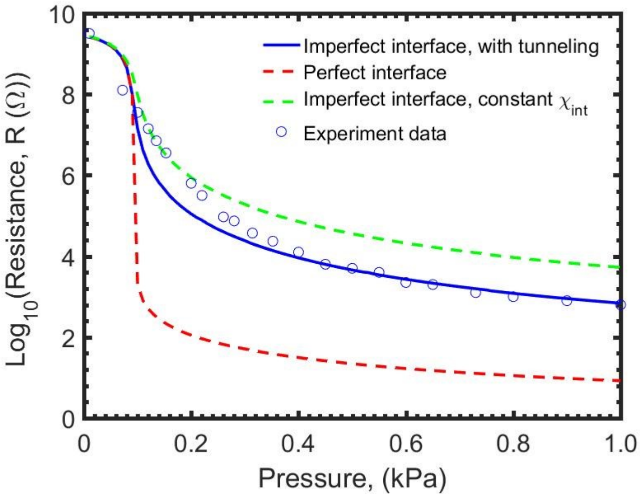

Fig.13. The resistance response of graphene/CNT/THV-based sensor under bending. Experiments from Lee et al. [35].

We now change the amount of CNTs inside the three-phase composite to see how CNTs influence the overall resistance under the same bending condition. From Fig. 14 we can see that, even a very small change of CNT volume fraction can cause a huge difference in overall resistance and percolation threshold. From Eq. (23), we know that the percolation threshold for graphene depends on the amount of CNTs, and thus, if we remove CNTs from the composite we can get a slightly higher percolation threshold for graphene and a little different conductivity curve, as Fig. 11 already indicated. Although it is very close to true case in Fig. 11, our three-phase composite sensor is pressure-sensitive, and changes of volume fractions of inclusion phases, though in a small range under the bending, can still lead to totally different resistance versus pressure curves, as Fig. 14 indicated. With the increase of the amount of CNTs, percolation threshold for graphene decreases, making the percolation occurring earlier and at less corresponding pressure. This finally influences the value of overall resistance significantly under the same external bending pressure.

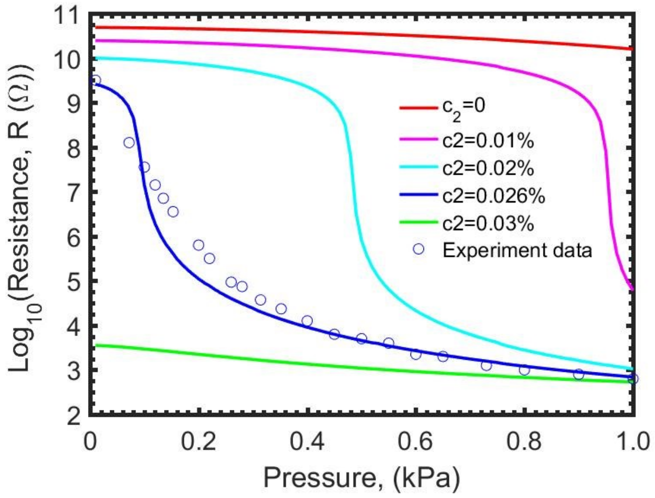

Fig.14. The different resistance of sensor under bending with different amounts of CNTs. Experiments from Lee et al. [35].

Recalling that the resistors-in-parallel model was adopted when we calculate the overall resistance of the bent sensor, it is instructive to provide a comparison curve that does not consider resistors in parallel. In Fig. 15, the green dashed curve represents the calculated resistance by treating the bent sensor as one resistor with a constant length, say, the initial length of composite sensor 9cm, and the blue solid line is from the suggested resistors-in-parallel model. They are very close to each other, which indicates that the two models do not have significant difference on the overall resistance. This is because the length of our composite sensor is much larger than its thickness, leading to very small changes on the effective lengths of different layers that will be taken into account in overall resistance calculation. But compared to treating the bent sensor as one single resistor, the resistors-in-parallel model should give a more precise result.

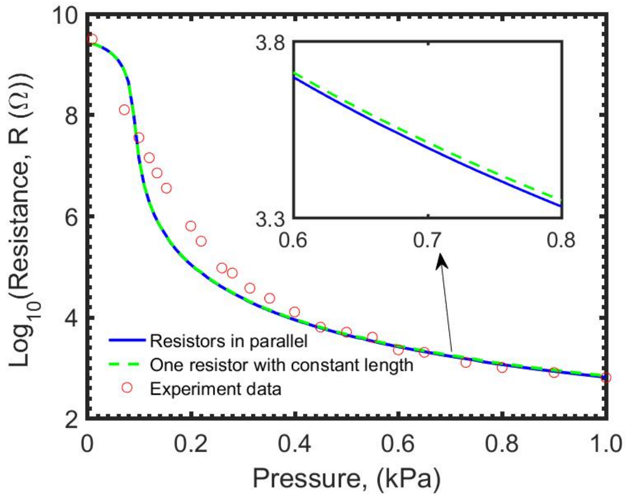

Fig.15. Comparison of considering resistors-in-parallel model with a single-resistor model. Experiments from Lee et al. [35].

3.4 Application of the theory to two-phase CNT/THV nanocomposite-based pressure sensor

Apart from the three-phase graphene/CNT/THV nanocomposite pressure sensor, the experiments of Lee et al. [35] also reported pressure-sensing results for the two-phase CNT/THV pressure sensor. In this last section, we demonstrate the application of the developed theory to this case by setting the graphene volume fraction, $c_1 = 0$ in all calculations, and c_2 is reset as 1.49% (1wt%) according to the experiment data. First, with the increase of applied pressure from zero to 1.8 kPa, the change of CNT volume fraction was obtained as shown in Fig. 16.

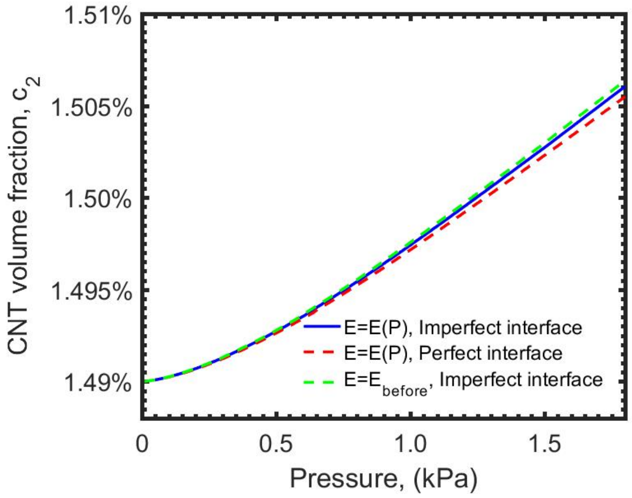

Fig.16. The change in CNT volume fraction in CNT/THV composite under bending.

With the CNT volume fraction so updated, the results of overall resistance versus the applied pressure during bending was calculated, as shown in Fig. 17. The calculations included the conditions of perfect interface (dashed red lines), imperfect interface without electron tunneling (dashed green line), and the complete interfacial conditions with imperfect bonding and electron tunneling (solid blue line). The sharp decrease of resistance is evident with the applied pressure, most notably around 0.1-0.15kPa. Just after applying the pressure, the percolation occurs inside the composite, which means that the percolation threshold is only a little more than the initial CNT volume fraction 1.49%. According to Eq. (24) and the CNT aspect ratio $\alpha_2 = 30.2$, our calculated percolation threshold is 1.492%, which fits well with the experimental behavior.

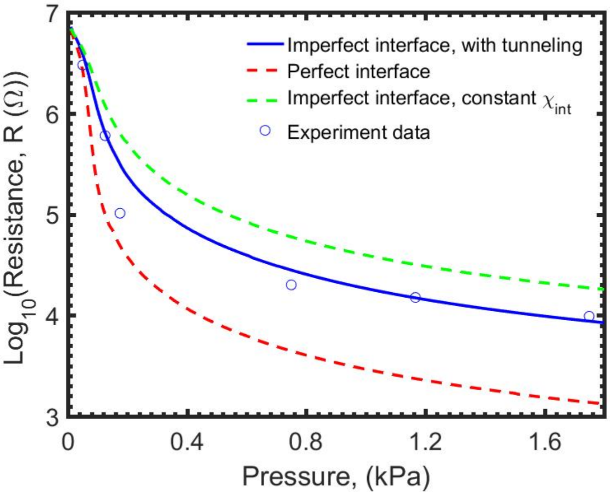

Fig.17. The resistance response of CNT/THV-based sensor under bending. Experiments from Lee et al. [35].

4 CONCLUSIONS

In this paper, we have established a comprehensive theory to calculate the elastic stiffness and electrical conductivity of a hybrid graphene/CNT/polymer nanocomposite sensor during the bending process. A key finding is that the volume fractions of graphene nanoplatelets and CNTs increase with the bending curvature, and this increase in turn leads to the sharp decrease in electrical resistance once the bending force is applied. The explicit relationship between external bending pressure and resistance of pressure sensor is given. With the increase of the pressure, resistance reduced by several orders of magnitude, which makes pressure sensor conductive from an insulator. The theoretical origin of this remarkable outcome is believed to be first reported in the literature. It can have significant implications on the applications of nanofiller-reinforced polymer composites in pressure sensing.

In the calculations of elastic stiffness, in particular, the effective Young's modulus, of the three-phase graphene/CNT/polymer nanocomposite, the influence of volume fractions of graphene nanoplatelets and CNTs, and their transversely anisotropic behavior, are fully accounted for, under both perfect and imperfect interface conditions. The growth of graphene and CNT volume fractions, and the change of bending curvature of the composite sensor as the applied pressure increases, are demonstrated. In the electrical setting, the effective conductivity and percolation threshold of the three-phase nanocomposite are fully addressed with full consideration of imperfect interfacial bonding and electron tunneling. In addition, a resistors-in-parallel model is also proposed to calculate the effective resistance of the pressure sensor. The calculated conductivity and percolation threshold, and the decrease of resistance for the three-phase graphene/CNT/THV nanocomposite as the applied pressure increases, are shown to be in accordance with the experimental data. The theory has also been applied to the two-phase CNT/THV nanocomposite. The calculated resistance is found to decrease markedly as the applied pressure increases.

The outcomes of these studies have pointed to the direction that the hybrid three-phase composite is exactly a very novel and valuable material compared to the traditional two-phase nanocomposites that contain just graphene or just CNTs. The mechanism on conductance enhancement of two inclusion phases is more significant compared to a single inclusion phase. From our theory, we can clearly see exactly how percolation occurs inside the graphene/CNT/polymer composite owing to the increase of graphene fillers and CNTs, and how both two inclusion phases determine the overall percolation threshold and electrical conductivity. Moreover, these two inclusion phases influence each other's respective percolation threshold. The percolation threshold for graphene fillers decreases with the addition of CNTs, and this phenomenon also applies to percolation threshold for CNTs after adding graphene. Based on this trait, the nanofiller pressure sensor made of graphene/CNT/polymer composite exhibits more sensitivity to pressure and lower electrical resistance. More importantly, since we can obtain the elastic and electrical responses for a given sensor, we can inversely use our theory to design piezoresistive sensors. To meet with the specific desired working pressure, resistance responses and sensitivity range in industry, we can predict the geometry and weight (or volume) concentrations of each component in this kind of nanofiller-polymer based sensors. This can provide new ideas for the development of more novel and ideal piezoresistive sensors in industrial production.

Appendix

For an ellipsoidal inclusion embedded into polymer matrix with the symmetric axis identified as x_1, the components of its Eshelby tensor in mechanical domain are given as

$$S_{1111} = \frac{1}{2(1-\nu_0)}\left\{1-2\nu_0+\frac{3\alpha^2-1}{\alpha^2-1}-\left[1-2\nu_0+\frac{3\alpha^2}{\alpha^2-1}\right]g(\alpha)\right\} \tag{A.1}$$

$$S_{2222} = S_{3333} = \frac{3}{8(1-\nu_0)}\frac{\alpha^2}{\alpha^2-1}+\frac{1}{4(1-\nu_0)}\left[1-2\nu_0-\frac{9}{4(\alpha^2-1)}\right]g(\alpha) \tag{A.2}$$

$$S_{2233} = S_{3322} = \frac{1}{4(1-\nu_0)}\left\{\frac{\alpha^2}{2(\alpha^2-1)}-\left[1-2\nu_0+\frac{3}{4(\alpha^2-1)}\right]g(\alpha)\right\} \tag{A.3}$$

$$S_{2211} = S_{3311} = -\frac{1}{2(1-\nu_0)}\frac{\alpha^2}{\alpha^2-1}+\frac{1}{4(1-\nu_0)}\left[\frac{3\alpha^2}{\alpha^2-1}-(1-2\nu_0)\right]g(\alpha) \tag{A.4}$$

$$S_{1122} = S_{1133} = -\frac{1}{2(1-\nu_0)}\left(1-2\nu_0+\frac{1}{\alpha^2-1}\right)+\frac{1}{2(1-\nu_0)}\left[1-2\nu_0+\frac{3}{2(\alpha^2-1)}\right]g(\alpha) \tag{A.5}$$

$$S_{2323} = \frac{1}{4(1-\nu_0)}\left\{\frac{\alpha^2}{2(\alpha^2-1)}+\left[1-2\nu_0-\frac{3}{4(\alpha^2-1)}\right]g(\alpha)\right\} \tag{A.6}$$

$$S_{1212} = S_{1313} = \frac{1}{4(1-\nu_0)}\left\{1-2\nu_0-\frac{\alpha^2+1}{\alpha^2-1}-\frac{1}{2}\left[1-2\nu_0-\frac{3(\alpha^2+1)}{\alpha^2-1}\right]g(\alpha)\right\} \tag{A.7}$$

where $g(\alpha)$ is given by $g(\alpha)=\left[\alpha/(1-\alpha^2)^{3/2}\right]\cdot\left[\operatorname{acos}(\alpha)-\alpha(1-\alpha^2)^{1/2}\right]$ when inclusion is oblate like graphene; and $g(\alpha)=\left[\alpha/(\alpha^2-1)^{3/2}\right]\cdot\left[\alpha(\alpha^2-1)^{1/2}-\operatorname{acosh}(\alpha)\right]$ when inclusion is prolate like CNT. When we calculate the Eshelby tensor components of graphene-THV interface and CNT-THV interface, just replace ν_0 in above expressions by ν_{int}^{GNP} and ν_{int}^{CNT} respectively.

The conversions between the elastic stiffness tensor components and Young's modulus and Poisson's ratio of isotropic medium can be expressed as

$$k_i=\frac{E_i}{2(1-2\nu_i)(1+\nu_i)} \tag{A.8}$$

$$l_i=\frac{E_i\nu_i}{(1-2\nu_i)(1+\nu_i)} \tag{A.9}$$

$$n_i=\frac{E_i(1-\nu_i)}{(1-2\nu_i)(1+\nu_i)} \tag{A.10}$$

$$m_i=p_i=\frac{E_i}{2(1+\nu_i)} \tag{A.11}$$

where subscript "i" can be 0 to represent the isotropic polymer matrix phase or can be "int" to represent the isotropic graphene-THV interface and CNT-THV interface.

Acknowledgements

X.D. Xia thanks the support of National Natural Science Foundation of China (Grant No. 11902365), Natural Science Foundation of Hunan Province (Grant No. 2020JJ5685) and the Alexander von Humboldt Research Fellowship. A. D. Mazzeo acknowledges the support of NSF ECCS- 1653584. G.J. Weng and A. D. Mazzeo acknowledge the support of NSF ECCS-1610933. G. J. Weng acknowledges the support of NSF CMMI-1162431. J. W. Shan acknowledges the support of Army STTR W911NF-20-P-0004 and Air Force STTR FA864922P0554.

References

[1] Park J, Lee Y, Hong J, Ha M, Jung YD, Lim H, Kim SY, Ko H. Giant tunneling piezoresistance of composite elastomers with interlocked microdome arrays for ultrasensitive and multimodal electronic skins. ACS Nano 2014;8:4689–97.

[2] Yang J, Xu Y, Guo Q, Yin F, Yuan W. Highly stretchable pressure sensors with wrinkled fibrous geometry for selective pressure sensing with minimal lateral strain-induced interference. Composites Part B 2021;217:108899.

[3] Li T, Luo H, Qin L, Wang X, Xiong Z, Ding H, Gu Y, Liu Z, Zhang T. Flexible capacitive tactile sensor based on micropatterned dielectric layer. Small 2016;12:5042–8.

[4] Son D, Lee J, Qiao S, Ghaffari R, Kim J, Lee JE, Song C, Kim SJ, Lee DJ, Jun SW, Yang S. Multifunctional wearable devices for diagnosis and therapy of movement disorders. Nat Nanotechnol 2014;9:397–404.

[5] Li B, Luo J, Huang X, Lin L, Wang L, Hu M, Tang L, Xue H, Gao J, Mai YW. A highly stretchable, super-hydrophobic strain sensor based on polydopamine and graphene reinforced nanofiller composite for human motion monitoring. Composites Part B 2020;181:107580.

[6] Yang Y, Zhang H, Lin ZH, Zhou YS, Jing Q, Su Y, Yang J, Chen J, Hu C, Wang ZL. Human skin based triboelectric nanogenerators for harvesting biomechanical energy and as self-powered active tactile sensor system. ACS Nano 2013;7:9213–22.

[7] Mannsfeld SC, Tee BC, Stoltenberg RM, Chen CV, Barman S, Muir BV, Sokolov AN, Reese C, Bao Z. Highly sensitive flexible pressure sensors with microstructured rubber dielectric layers. Nat Mater 2010;9:859–64.

[8] Mandal D, Yoon S, Kim KJ. Origin of piezoelectricity in an electrospun poly (vinylidene fluoride-trifluoroethylene) nanofiller web-based nanogenerator and nano-pressure sensor. Macromol Rapid Commun 2011;32:831–7.

[9] Pan L, Chortos A, Yu G, Wang Y, Isaacson S, Allen R, Shi Y, Dauskardt R, Bao Z. An ultra-sensitive resistive pressure sensor based on hollow-sphere microstructure induced elasticity in conducting polymer film. Nat Commun 2014;5:1–8.

[10] Tian H, Shu Y, Wang XF, Mohammad MA, Bie Z, Xie QY, Li C, Mi WT, Yang Y, Ren TL. A graphene-based resistive pressure sensor with record-high sensitivity in a wide pressure range. Sci Rep 2015;5:1–6.

[11] Al-Saygh A, Ponnamma D, AlMaadeed MA, Vijayan P P, Karim A, Hassan MK. Flexible pressure sensor based on PVDF nanocomposites containing reduced graphene oxide-titania hybrid nanolayers. Polymers 2017;9:33.

[12] Wu X, Han Y, Zhang X, Zhou Z, Lu C. Large-area compliant, low-cost, and versatile pressure-sensing platform based on microcrack-designed carbon black@ polyurethane sponge for human-machine interfacing. Adv Funct Mater 2016;26:6246–56.

[13] Feng C, Yi Z, Jin X, Seraji SM, Dong Y, Kong L, Salim N. Solvent crystallization-induced porous polyurethane/graphene composite foams for pressure sensing. Composites Part B 2020;194:108065.

[14] Zhao X, Chen B, Wei G, Wu JM, Han W, Yang Y. Polyimide/graphene nanocomposite foam-based wind-driven triboelectric nanogenerator for self-powered pressure sensor. Adv Mater Technol 2019;4:1800723.

[15] Hwang J, Kim Y, Yang H, Oh JH. Fabrication of hierarchically porous structured PDMS composites and their application as a flexible capacitive pressure sensor. Composites Part B 2021;211:108607.

[16] Tang J, Wu Y, Ma S, Yan T, Pan Z. Flexible strain sensor based on CNT/TPU composite nanofiller yarn for smart sports bandage. Composites Part B 2022;232:109605.

[17] Liang T, Zou X, Pal RK, Xie J, Assasie-Gyimah MK, Liu J, Guo W, Chen C, Tenorio M, Sullivan D, Root A. Tunable electrical properties of embossed, cellulose-based paper for skin-like sensing. ACS Appl Mater Interfaces 2020;12:51960–8.

[18] Hu B, Hu N, Li Y, Akagi K, Yuan W, Watanabe T, Cai Y. Multi-scale numerical simulations on piezoresistivity of CNT/polymer nanocomposites. Nanoscale Res Lett 2012;7:1–1.

[19] Sepúlveda AT, Fachin F, de Villoria RG, Wardle BL, Viana JC, Pontes AJ, Rocha LA. Nanocomposite flexible pressure sensor for biomedical applications. Procedia Engineering 2011;25:140–3.

[20] Stankovich S, Dikin DA, Dommett GHB, Kohlhaas KM, Zimney EJ, Stach EA, Piner RD, Nguyen ST, Ruoff RS. Graphene-based composite materials. Nature 2006;442:282–6.

[21] Li D, Müller MB, Gilje S, Kaner RB, Wallace GG. Processable aqueous dispersions of graphene nanosheets. Nat Nanotechnol 2008;3:101–5.

[22] Yang J, Luo S, Zhou X, Li J, Fu J, Yang W, Wei D. Flexible, tunable, and ultrasensitive capacitive pressure sensor with microconformal graphene electrodes. ACS Appl Mater

Interfaces 2019;11:14997–5006.

[23] Lou Z, Chen S, Wang L, Jiang K, Shen G. An ultra-sensitive and rapid response speed graphene pressure sensors for electronic skin and health monitoring. Nano Energy 2016;23:7–14.

[24] Hwang S-H, Park HW, Park Y-B. Piezoresistive behavior and multi-directional strain sensing ability of carbon nanotube–graphene nanoplatelet hybrid sheets. Smart Mater Struct 2012;22:015013.

[25] Lee C, Jug L, Meng E. High strain biocompatible polydimethylsiloxane-based conductive graphene and multiwalled carbon nanotube nanocomposite strain sensors. Appl Phys Lett 2013;102:183511.

[26] Tran MT, Tung TT, Sachan A, Losic D, Castro M, Feller JF. 3D sprayed polyurethane functionalized graphene/carbon nanotubes hybrid architectures to enhance the piezo-resistive response of quantum resistive pressure sensors. Carbon 2020;168:564–79.

[27] Peng S, Li L, Han X, Sun W, Srinivasan M, Mhaisalkar SG, Cheng F, Yan Q, Chen J, Ramakrishna S. Cobalt sulfide nanosheet/graphene/carbon nanotube nanocomposites as flexible electrodes for hydrogen evolution. Angew Chem 2014;126:12802–7.

[28] Shen L, Zhang X, Li H, Yuan C, Cao G. Design and tailoring of a three-dimensional TiO2–graphene–carbon nanotube nanocomposite for fast lithium storage. J Phys Chem Lett 2011;2:3096–101.

[29] Wang Y, Weng GJ, Meguid SA, Hamouda AM. A continuum model with a percolation threshold and tunneling-assisted interfacial conductivity for carbon nanotube-based nanocomposites. J Appl Phys 2014;115:193706.

[30] Xia X, Hao J, Wang Y, Zhong Z, Weng GJ. Theory of electrical conductivity and dielectric permittivity of highly aligned graphene-based nanocomposites. J Phys Condens Matter 2017;29:205702.

[31] Du H, Spratford S, Shan JW, Weng GJ. Experimental and theoretical study of the evolution of fluid-suspended graphene morphology driven by an applied electric field and the attainment of ultra-low percolation threshold in graphene-polymer nanocomposites. Compos Sci Technol 2020;199:108315.

[32] Mori T, Tanaka K. Average stress in matrix and average elastic energy of materials with misfitting inclusions. Acta Metall 1973;21:571–4.

[33] Qiu YP, Weng GJ. On the application of Mori-Tanaka's theory involving transversely isotropic spheroidal inclusions. Int J Eng Sci 1990;28:1121–37.

[34] Bruggeman DAG. Calculation of various physics constants in heterogenous substances. I Dielectricity constants and conductivity of mixed bodies from isotropic substances. Ann Phys 1935;24:636–64.

[35] Lee S, Reuveny A, Reeder J, Lee S, Jin H, Liu Q, Yokota T, Sekitani T, Isoyama T, Abe Y, Suo Z. A transparent bending-insensitive pressure sensor. Nat Nanotechnol 2016;11:472–8.

[36] Hill R. Theory of mechanical properties of fibre-strengthened materials: I. Elastic behaviour. J Mech Phys Solids 1964;12:199–212.

[37] Weng GJ. Some elastic properties of reinforced solids, with special reference to isotropic ones containing spherical inclusions. Int J Eng Sci 1984;22:845–56.

[38] Landauer R. The electrical resistance of binary metallic mixtures. J Appl Phys 1952;23:779–84.

[39] Weng GJ. A dynamical theory for the Mori–Tanaka and Ponte Castañeda–Willis estimates. Mech Mater 2010;42:886-893.

[40] Landau, LD, Lifshitz, EM. Electrodynamics of continuous media (1st edition). Elsevier, Amsterdam (in English) 1960.

[41] Cadelano E, Palla PL, Giordano S, Colombo L. Elastic properties of hydrogenated graphene. Phys Rev B Condens Matter 2010;82:235414.

[42] Hashemi R. On the overall viscoelastic behavior of graphene/polymer nanocomposites with imperfect interface. Int J Eng Sci 2016;105:38–55.

[43] Shen L, Li J. Transversely isotropic elastic properties of single-walled carbon nanotubes. Phys Rev B Condens Matter 2004;69:045414.

[44] Zhang S, Koziol KK, Kinloch IA, Windle AH. Macroscopic fibers of well-aligned carbon nanotubes by wet spinning. Small 2008;4:1217–22.

Table 1. Parameters and physical values used in mechanical part (graphene properties taken from Cadelano et al. [41] and Hashemi [42] and CNT properties from Shen and Li [43])

Plane-strain bulk modulus of graphene, k_1 (GPa)	6.1×10^{2}
Cross modulus of graphene, l_1 (GPa)	15
Axial modulus of graphene, n_1 (GPa)	36.9
Transverse shear modulus of graphene, m_1 (GPa)	4.3×10^{2}
Axial shear modulus of graphene, p_1 (GPa)	4
Plane-strain bulk modulus of CNT, k_2 (GPa)	2.7×10^{2}
Cross modulus of CNT, l_2 (GPa)	86.4
Axial modulus of CNT, n_2 (GPa)	1.1×10^{3}
Transverse shear modulus of CNT, m_2 (GPa)	17
Axial shear modulus of CNT, p_2 (GPa)	4.4×10^{2}
Young's modulus of graphene-THV interface, E_{int}^{GNP} (GPa)	20
Poisson's ratio of graphene-THV interface, ν_{int}^{GNP}	0.33
Young's modulus of CNT-THV interface, E_{int}^{CNT} (GPa)	1.0×10^{2}
Poisson's ratio of CNT-THV interface, ν_{int}^{CNT}	0.33

Table 2. Parameters and physical values used in electrical part (graphene properties taken from Stankovich et al. [20] and CNT properties from Zhang et al. [44])

Out-of-plane electrical conductivity of graphene filler, χ_1^{GNP} (Sm^{-1})	1.0×10^2
In-plane electrical conductivity of graphene filler, χ_3^{GNP} (Sm^{-1})	1.0×10^5
Axial electrical conductivity of CNT, χ_1^{CNT} (Sm^{-1})	3.0×10^4
Transverse electrical conductivity of CNT, χ_3^{CNT} (Sm^{-1})	30
Intrinsic electrical conductivity of graphene-THV interface, $\chi_0^{(\mathrm{int})GNP}$ (Sm^{-1})	2.0
Intrinsic electrical conductivity of CNT-THV interface, $\chi_0^{(\mathrm{int})CNT}$ (Sm^{-1})	0.2
Electronic tunneling scale parameter at graphene-THV interface, γ_1	1.5×10^{-4}
Electronic tunneling scale parameter at CNT-THV interface, γ_2	1.0×10^{-4}